Constriction Resistance and Current Crowding in Electrically Pumped Semiconductor Nanolasers with the Presence of Undercut and Sidewall Tilt

Peng Zhang, *Member, IEEE*, Qing Gu, Y. Y. Lau, *Fellow, IEEE*, and Yeshaiahu Fainman, *Fellow, IEEE*

Abstract—We evaluate the constriction resistance and current crowding in nanolasers using the finite-element method based calculations. We examine both the vertical contact and horizontal contact structures, representing the typical top contact and bottom contact of nanolasers, respectively. We find that, in general, constriction resistance and the degree of current crowding in the bottom horizontal contact in nanolasers are much larger than those in the top vertical contact. For both contacts, constriction resistance and, therefore, the degree of current crowding increase as the nanolaser radius decreases, the amount of undercut increases, or the angle (either positive or negative) of the sidewall tilt increases. The location where most current crowding and most Joule heating occur is identified. The results may provide insights into the design optimization of nanolasers.

Index Terms—Semiconductor nanolasers, nanoscale devices, contact resistance, constriction resistance, current crowding, thermal management, joule heating.

I. INTRODUCTION

NANOLASERS generally refer to lasers whose mode volume is smaller than λ_0^3, where λ_0 is the emission wavelength in free space. In the more strict definition, nanolasers should also have physical sizes that's sub-wavelength in all three dimensions [1], [2]. For semiconductor nanolasers, the latter requirement is particularly relevant because of their envisioned application in chip-scale optical communications, which promises data rates beyond that feasible in the realm of electronics [2], [3]. The first and foremost challenge in realizing nanolasers is to have enough material gain to reach lasing threshold, which typically increases as the laser size is decreased. As a result, most of the

earlier proof-of-the-concept work was performed at cryogenic temperatures and/or under pulsed optical pumping, under which condition the loss is minimized [4]–[10]. However, the eventual insertion of semiconductor nanolasers into chip-scale circuits requires room temperature operation, continuous wave electrical injection of carriers, low threshold current and minimal self-heating. Continuous effort has been made in this direction, marked by the first electrically pumped metal-clad nanolaser operating at room temperature [9]. However, while thermal dynamics in vertical-cavity surface-emitting lasers (VCSELs) has been studied in depth [11], [12], it has been overlooked in nanolasers until recently. Recent efforts in understanding temperature effects in nanolasers include the exploration of different dielectric cladding materials to minimize self-heating [10], [13]; the multi-physics consideration of optical, electrical and thermal properties in the nanolaser design [10]; the evaluation of temperature's effect on figure-of-merits in nanolasers such as the Purcell factor, the spontaneous emission factor and the lasing threshold [14], [15].

For electrically pumped nanolasers, because of the limited contact area between an electrode and the cavity, implementing low-resistance and Ohmic electrodes is of crucial importance in minimizing self-heating. This is in part done in nanofabrication, by choosing the optimal thicknesses of contact metals and performing rapid thermal annealing after metal deposition. Additionally, adequate understanding of the performance of electrodes in a nanolaser can be of great aid in understanding the laser performance, and in so doing, aid in the optimization of cavity design.

In electrical simulations, Ohmic contact and uniform current spreading into the semiconductor material is usually assumed. In reality however, not only is the contact resistance not negligible, neither is the current spreading uniform. In particular, the geometrical shape of the semiconductor material will affect both these parameters, and it is expected that some trade-off exist between electrical and optical mode performance. Without loss of generality, we examine nanopillar cavities without and with InP undercut, schematically shown in Figure 1(a) and (b), respectively. Both designs have been used in electrically pumped nanolaser design [9], [10], [16]. In the case of an undercut design, Figure 1(b) presents the ideal vertical InP pedestals sidewall (noted as 0 degree). In practice, sidewall angles can vary from −20 to 20 degrees due to fabrication variations. Reference [17] analyzed how the various pedestal sidewall angles affect the nanolaser's optical
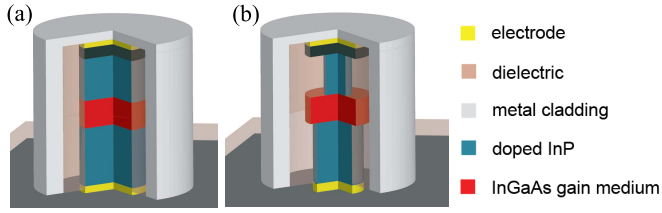
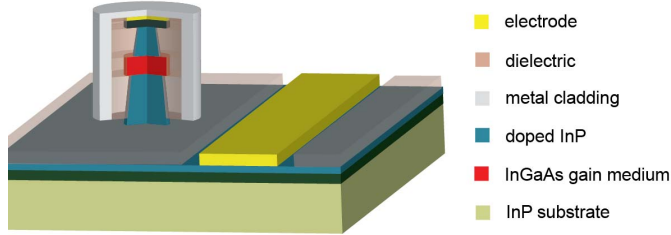Fig. 1. Schematic of a nanolaser (a) without, and (b) with InP undercut.

Fig. 2. Approximate sketch of nanolasers used in [5].

and thermal properties assuming the ideally Ohmic electrodes, but it is not yet understood how the sidewall angle would affect the contact resistance and current spreading, which will in turn affect the optical and thermal performance of the laser. The latter issue motivated our present study. Our study provides quantitative analysis to the thermal management of electrically pumped nanolasers, where self-heating is one of the main failure mechanisms. A validation of simulation with analytic theory is reported.

Typically, a nanolaser has a small-area top electrode that is in direct contact with the optical cavity and is comparable in size to the laser dimension (schematically shown in Fig. 1), and current flows vertically from the top electrode into the laser. It also has a large-area bottom electrode that can be shared among a number of devices on the same chip (schematically shown in Fig. 2), and current flow into the bottom of the laser can be either horizontal or vertical, depending on the resistances of the various substrate layers. Sometimes, both electrodes can be small-area electrodes in direct contact with the optical cavity (Fig. 1) [1] or large-area electrodes that are remotely connected to the optical cavity [2], under which condition the same contact resistance and current spreading analysis can be applied to both electrodes.

In this paper, we study the effects of tilted sidewalls on the electrical constriction resistance and current crowding, using the finite element method (FEM) based code, MAXWELL 2D [18], which is verified to give sufficiently accurate results in our previous works on spreading resistance [19]–[21]. In Sec. II, we analyze the resistance for the vertical contact structures in nanolasers, for the top contact above the gain region (Fig. 1), by considering various amount of undercut and sidewall tilt angle. In Sec. III, we then calculate the resistance and current density distribution for the bottom contact (Fig. 2), which is typically a horizontal contact structure. The effects of non-uniform spreading of current in the bottom thin film will be evaluated. Concluding remarks are given in Sec. IV.
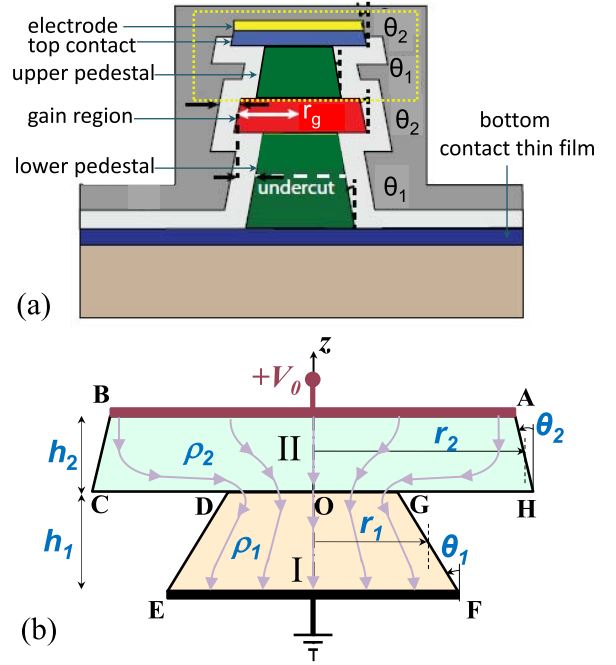

Fig. 3. (a) Nanolaser to be analyzed in 2D sideview, (b) Vertical contact above the gain region (dashed box region in (a)) with tilted sidewalls, with both angles of sidewall tilt θ_1 and θ_2 (both positive as shown). The z-axis is the axis of rotation for the cylindrical geometry.

II. VERTICAL CONTACT STRUCTURE

To study the vertical contact structure, which is above the gain region in nanolasers of Fig. 3a, we consider the simplified geometry of the vertical contact, shown in Fig. 3b. Regions I and II may represent the upper pedestal region and the top contact region in Fig. 3a, respectively. Following Ref. [17], we define the angles of the sidewall tilt (counterclockwise respect to the vertical axis) of regions I and II to be θ_1 and θ_2, respectively. Region I has average radius r_1, thickness h_1, and resistivity ρ_1, whereas Region II has average radius r_2, thickness h_2, and resistivity ρ_2. The average radius of region II (top electrode) r_2 is usually assumed to be the same as that of the gain region (Fig. 3a).

The total resistance from AB to EF in Fig. 3b is,

$$R = R_I + R_c + R_{II}, \tag{1}$$

where R_I and R_{II} are the bulk resistance of region I from DG to EF and of Region II from AB to CH, respectively. They are defined as,

$$R_I = \frac{\rho_1 h_1}{\pi} \frac{1}{r_1^2 - (h_1^2/4)\tan^2\theta_1}, \tag{2a}$$

$$R_{II} = \frac{\rho_2 h_2}{\pi} \frac{1}{r_2^2 - (h_2^2/4)\tan^2\theta_2}, \tag{2b}$$

and

$$R_c = \frac{\rho_2}{4a}\bar{R}_c, \tag{2c}$$

is the additional constriction resistance due to current crowding effects at the interface between regions I and II in Fig. 3b, where $a = r_1 - 0.5 h_1 \tan\theta_1$ is the radius of contact interface OG.

Note that if θ_1 and θ_2 become zero, there would be no sidewall tilt in the contact members and Eq. (2) would reduce to that of cylinders. For the case of zero sidewall tilt, the normalized constriction resistance $\bar{R}_c$ is calculated *exactly* in Ref. [21] and is given by,

$$\bar{R}_c \left(\frac{r_1}{r_2}, \frac{h_1}{r_1}, \frac{r_1}{h_2}, \frac{\rho_1}{\rho_2} \right) = \frac{8}{\pi} \frac{\rho_1}{\rho_2} \sum_{n=1}^{\infty} B_n \sinh(\beta_n h_2) \frac{J_1(\beta_n r_1)}{\beta_n r_1},$$

(3)

for arbitrary values of r_1, r_2 ($r_2 > r_1$), h_1, h_2 and ρ_1/ρ_2, where B_n is calculated from [21, eq. (B4)], β_n satisfies $J_1(\beta_n r_2) = 0$, and $J_1(x)$ is the Bessel function of order one.

In the more general case when θ_1 and θ_2 are non-zero, instead of using an analytical expression, we obtain the constriction resistance R_c from Eqs. (1) and (2) after knowing the total resistance R by the voltage-to-current ratio, for the structure in Fig. 3b. We use dimensions and resistivities in typical nanolasers based on epitaxially-grown wafer stack in previous work [17], [22]. Unless otherwise stated, in our calculation, we fix the following parameters in Fig. 3b as $h_1 = 470$ nm, $h_2 = 125$ nm, $\rho_1 = 1/\sigma_1 = 1/1.001 \times 10^5$ S/m $= 1 \times 10^{-5}$ Ωm, $\rho_2 = 1/\sigma_2 = 1/8.011 \times 10^5$ S/m $= 1.248 \times 10^{-6}$ Ωm [22].

Figure 4a shows the constriction resistance R_c as a function of the amount of undercut, defined as $(r_2 - r_1)/r_2$, for different radius $r_2 = 775$nm, 550nm, and 225nm, for the case of zero sidewall tilt. It is clear that R_c increases as the amount of undercut increases, indicating more severe current crowding at the interface. The effect of undercut on the constriction resistance is more profound for smaller gain radius. The MAXWELL numerical calculations are compared with our analytical results obtained from Eqs. (2c) and (3) for $\theta_1 = \theta_2 = 0$. As seen from Fig. 4a, excellent agreement is obtained. Figure 4b shows R_c as a function of the angle of sidewall tilt θ_1 of region I for the case $r_2 = 550$ nm, under different amount of undercut. Figure 4c shows R_c as a function of θ_1 for an fixed undercut = 20%, for different radius r_2. The constriction resistance R_c increases significantly as θ_1 deviates from zero. For larger amount of undercut (Fig. 4b) or smaller radius (Fig. 4c), the increase of R_c is even more sensitive to the region I sidewall tilt angle θ_1. The sidewall tilt of region II θ_2 is also expected to increase the constriction resistance R_c. However, since region II is highly conductive compared to region I, $\rho_2/\rho_1 \sim 0.1$, the increase of R_c with θ_2 is almost negligible, as shown in Fig. 4d. It is important to note that the constriction resistance is typically smaller than the bulk resistance of regions I and II, $R_c < R_I, R_{II}$. For the cases studied in Fig. 4, the ratio of constriction resistance to total resistance R_c/R_{tot} is 16% at most. However, the current density and heating near the current constricted region are significantly higher than those in the bulk region of I and II, as discussed below.

While the value of constriction resistance R_c contributes to total resistance due to current crowding, it is important to identify where the most current crowding occurs in a contact structure. Figure 5 shows the current density distribution $J(r, z)$ for the vertical contact structure in Fig. 3b with
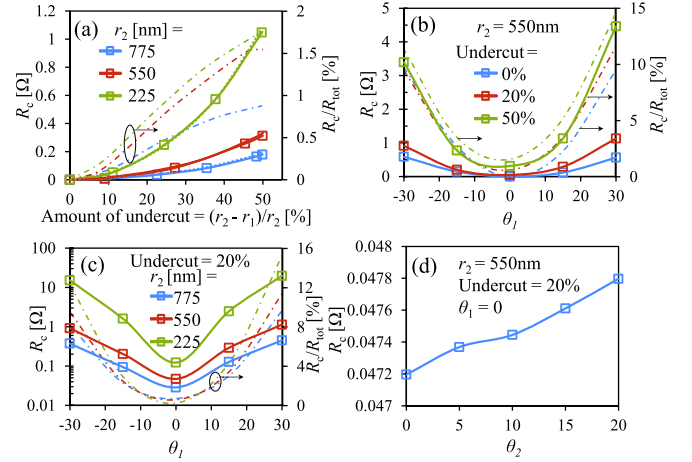

Fig. 4. Constriction resistance R_c for vertical contact structure in Fig. 3b, as a function of (a) amount of undercut = $(r_2 - r_1)/r_2$, for the case of zero sidewall tilt $\theta_1 = \theta_2 = 0°$, for $r_2 = 775$nm, 550 nm, and 225 nm; (b) angle of sidewall tilt of region I θ_1, for $r_2 = 550$ nm, with amount of undercut = 0%, 20%, and 50%; (c) θ_1, with amount of undercut = 20%, for $r_2 = 775$nm, 550 nm, and 225 nm; (d) angle of sidewall tilt of region II θ_2, for the case of $r_2 = 550$ nm with amount of undercut = 20%. Symbols are for the numerical data from MAXWELL in (a) for analytical calculations from Eqs. (2c) and (3), and solid lines for curve connecting the numerical data. The dash-dotted lines are for the ratio of constriction resistance to total resistance R_c/R_{tot}. In (d), $R_c/R_{tot} \approx 0.6\%$.

the sidewall angle tilt $\theta_1 = 30°, 0°$, and $-30°$, for $r_2 = 550$ nm and amount of undercut = 50%. In the calculation, we assume a total injection current of 0.5mA, corresponding to a current density of $J_0 = 2.1$ nA/nm^2 in region I with zero sidewall tilt if uniform current distribution is assumed. As shown in Fig. 5a, when $\theta_1 = 30°$, severe current crowding occurs at the constriction corner point G, with a current density as high as 23.5 nA/nm^2 at 1 nm away from point G towards the center axis (right at point G the current density is infinity due to the mathematically sharp corner assumed), which is about 11 times J_0. On the other hand, the current density near the bottom rim of region I (point F) is suppressed. When $\theta_1 = 0°$ (Fig. 5b), the current crowding region become significantly smaller compared to that of $\theta_1 = 30°$, with a current density of 4.5 nA/nm^2 ($\sim 2J_0$) at 1 nm inwards from point G along the interface. When $\theta_1 = -30°$ (Fig. 5c), the current density is mostly crowed near the bottom surface of region I, with current density of 18.9 nA/nm^2 ($\sim 9J_0$) at 1 nm inwards from point F along the interface, whereas the current density near the interface between regions I and II become quite uniformly distributed. The magnitude of current density along the contact interface OH is shown in Fig. 5g for cases with different angle of tilt. It is important to note that, even though the constriction resistance $R_c = 3.39$ Ω for $\theta_1 = -30°$ and $R_c = 4.46$ Ω for $\theta_1 = 30°$ are comparable (c.f. Fig. 4b), the location where current crowding occurs is very different. Figures 5d-f show the corresponding distribution of Joule heating power per volume $P(r, z) = \rho(r, z)J^2(r, z)$. The total Joule heating power in the structures in Figs. 5d-f is 7.7, 5.1, and 7.4 μW, respectively, corresponding to an increase of 51% for $\theta_1 = 30°$ and 45% for $\theta_1 = -30°$ relative to the straight sidewall case $\theta_1 = 0°$. Though the total power is not increased much by sidewall tilt, the power density near the most current crowded
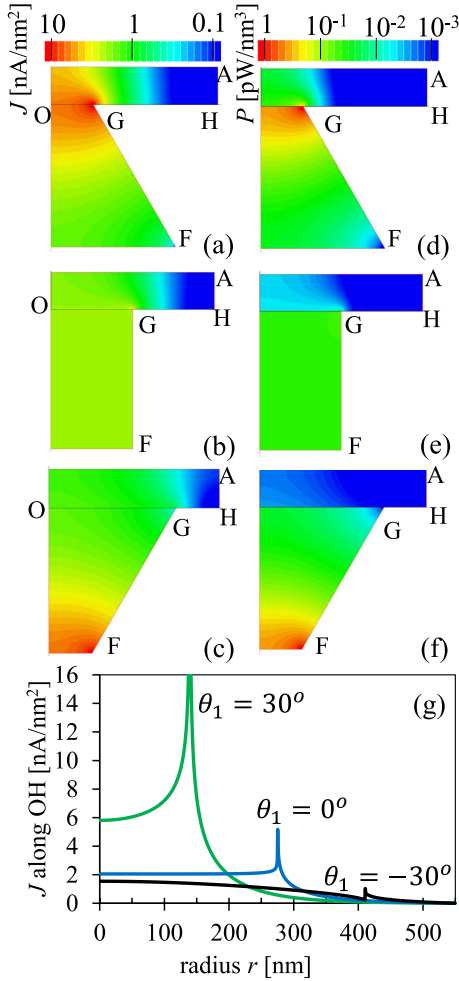
Fig. 5. (a)-(c) Current density distribution $J(r, z)$, and (d)-(f) the corresponding Joule heating power per volume $P(r, z) = \rho(r, z) J^2(r, z)$, for the vertical contact structure in Fig. 3b for $r_2 = 550$ nm and amount of undercut = 50%. (a) and (d) are for the sidewall angle tilt $\theta_1 = 30°$, (b) and (e) for $\theta_1 = 0°$, and (c) and (f) for $\theta_1 = -30°$. (g) magnitude of current density along OH for cases (a)-(c). In the calculation, we assume a total injection current of 0.5mA.

region is significantly increased. The hottest spot follows the region of highest current density closely, yielding $P \approx 3.4$, 0.085 and 3.8 pW/nm³ at 1nm away from the hottest corner for $\theta_1 = 30°$, 0°, and $-30°$, respectively, corresponding to an increase of P by 39 times for $\theta_1 = 30°$ and by 44 times for $\theta_1 = -30°$ relative to the case $\theta_1 = 0°$.

III. HORIZONTAL CONTACT STRUCTURE

To study the bottom contact region in nanolasers (Fig. 6a), we consider the geometry of horizontal contact, shown in Fig. 6b. Regions I and II represent the lower pedestal region and the bottom thin film region (Fig. 6a), respectively. Similar to Section II, we define the angle of the sidewall tilt in Region I to be θ_1. Region I has average radius r_1, thickness h_1, and resistivity ρ_1, whereas region II has average radius r_2 ($r_2 \gg r_1$), thickness h_2, and resistivity ρ_2.

The total resistance from EF to BC (and AH) in Fig. 6b is,

$$R = R_I + R_c + R_{II}, \qquad (4)$$
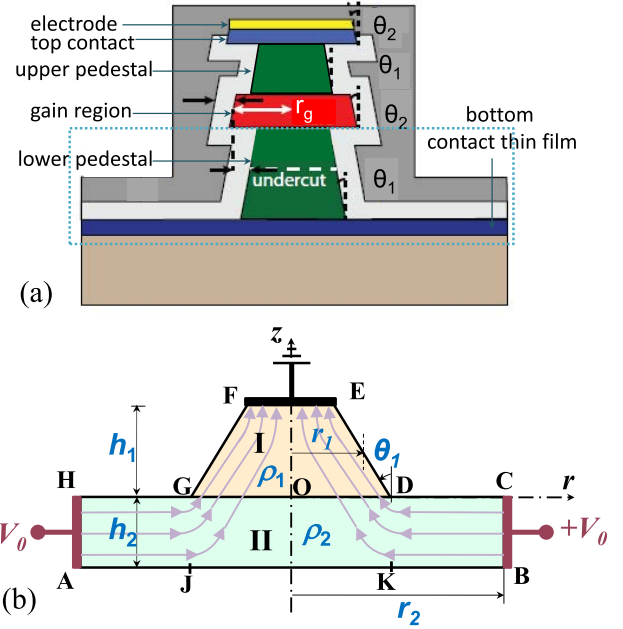

Fig. 6. (a) Nanolaser to be analyzed, (b) Horizontal contact below the gain region (dashed box region in (a)) with tilted sidewall of angle θ_1 (positive as shown). The radius of the gain region above region I is r_g. For zero undercut, $r_1 = r_g$. The z-axis is the axis of rotation for the cylindrical geometry.

where R_I is the bulk resistance of region I from EF to DG, and R_{II} is the bulk resistance of the bottom thin film disk in region II from DK to CB (and from GJ to HA), which are respectively defined as,

$$R_I = \frac{\rho_1 h_1}{\pi} \frac{1}{r_1^2 - (h_1^2/4) \tan^2 \theta_1}, \qquad (5a)$$

$$R_{II} = \frac{\rho_2}{2\pi h_2} ln\left[\frac{r_2}{r_1 + (h_1/2)\tan\theta_1}\right], \qquad (5b)$$

and

$$R_c = \frac{\rho_2}{4a} \bar{R}_c, \qquad (5c)$$

which includes the remaining resistance in the region GDJK, and more importantly the constriction resistance [19] due to current crowding effects at the interface between regions I and II in Fig. 6b, where $a = r_1 + 0.5h_1 \tan \theta_1$ is the radius of contact interface OD.

Note that if θ_1 becomes zero, there would be no sidewall tilt in region I and Eq. (5) would reduce to that of cylinders. For the case of zero sidewall tilt, the normalized constriction resistance $\bar{R}_c$ is calculated *exactly* in Ref. [20] and is given by,

$$\bar{R}_c\left(\frac{r_1}{r_2}, \frac{h_1}{r_1}, \frac{r_1}{h_2}, \frac{\rho_1}{\rho_2}\right) = \frac{8}{\pi} \frac{\rho_1}{\rho_2} \sum_{n=1}^{\infty} B_n \coth\left(\frac{\lambda_n h_2}{r_2}\right)$$
$$\times \frac{J_1(\lambda_n r_1/r_2)}{\lambda_n r_1/r_2} - \frac{2r_1}{\pi h_2} \ell n\left(\frac{r_2}{r_1}\right), \qquad (6)$$

for arbitrary values of r_1, r_2 ($>r_1$), h_1, h_2 and ρ_1/ρ_2, where B_n is calculated from Eq. (C4) of Ref. [20], λ_n satisfies $J_0(\lambda_n) = 0$, and $J_0(x)$ and $J_1(x)$ are the Bessel function of order zero and one, respectively.

In our numerical calculations, we obtain the total resistance R for the structure in Fig. 6b by the voltage-to-current ratio. We then obtain the constriction resistance R_c from Eqs. (4) and (5). We use dimensions and resistivities in typical nanolasers based on epitaxially-grown wafer stack in previous work [17], [22]. In our calculation, we fix the following parameters in Fig. 6b as $h_1 = 600$ nm, $h_2 = 135$ nm, $\rho_1 = 1/\sigma_1 = 1/2.803 \times 10^3$ S/m $= 3.568 \times 10^{-4}$ Ωm, $\rho_2 = 1/\sigma_2 = 1/1.602 \times 10^4$ S/m $= 6.2422 \times 10^{-5}$ Ωm. The bottom electrode is located at a distance far away from the nanolaser (Fig. 2), typically on the order of tens of μm. In the calculation, we fix $r_2 = 2$ μm in Fig. 6, because the current flow lines would become almost uniformly distributed at a distance beyond $2r_1$ from the contact constriction corner, when the contact dimension is larger than the bottom thin film thickness, OD $\geq h_2$ [20], [23]. Without any undercut, the average radius of region I should be the same as that of the gain region above region I (not shown in Fig. 6b), i.e. $r_1 = r_g$ for zero undercut (Fig. 1a). With undercut, r_1 is smaller than r_g, the amount of undercut here is defined as $(r_g - r_1)/r_g$.

Figure 7a shows the constriction resistance R_c as a function of the amount of undercut, for different gain radius $r_g = 775$nm, 550nm, and 225nm, for the case of zero sidewall tilt. R_c increases as the amount of undercut increases, indicating more severe current crowding at the interface. Similar to that seen for the vertical contact (Fig. 4a), the effect of undercut on the constriction resistance is more profound for smaller gain radius. In reported electrically pumped nanolasers [1], [9], [10], the semiconductor materials above the gain region is always n-doped and those below the gain region p-doped. As a result of the larger resistivity of p-doped materials in the bottom pedestal and bottom contact thin film, the constriction resistance is much larger compared to that in the top vertical contact (Fig. 7a vs. Fig. 4a). This is consistent with the previous study which reveals that the largest source of Joule heating is the lower pedestal, followed by the bottom contact [22]. The MAXWELL numerical calculations are compared with our analytical results obtained from Eqs. (5c) and (6). Excellent agreement is obtained, as shown in Fig. 7a. Figure 7b shows R_c as a function of angle of sidewall tilt θ_1 of region I for the case $r_g = 550$ nm, under different amount of undercut. Figure 7c shows R_c as a function of θ_1 for an undercut $= 20\%$, for different gain radius r_g. The constriction resistance R_c increases significantly as θ_1 deviates from zero. Similar to the vertical contact, for larger amount of undercut (Fig. 7b) or smaller radius (Fig. 7c), the increase in R_c is even more sensitive to θ_1. The constriction resistance is also typically smaller than the bulk resistance of regions I and II, $R_c < R_I, R_{II}$. For the cases studied in Fig. 7, the ratio of constriction resistance to total resistance R_c/R_{tot} is 16% at most. However, the current density and heating near the current constricted region are significantly higher than those in the bulk region of I and II.

It is important to examine where the most current crowding occurs. Figures 8a-c shows the current density distribution $J(r,z)$ for the horizontal contact structure in Fig. 6b of the sidewall angle tilt $\theta_1 = 30°$, $0°$, and $-30°$, respectively, for
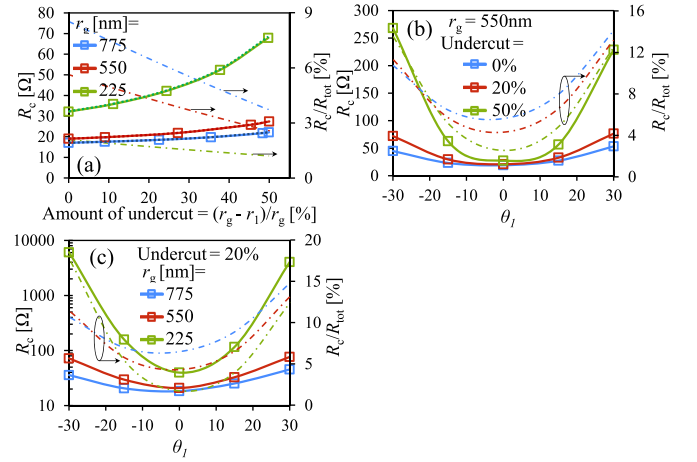

Fig. 7. Constriction resistance R_c for horizontal contact structure in Fig. 6b, as a function of (a) amount of undercut $= (r_g - r_1)/r_g$, for the case of zero sidewall tilt $\theta_1 = 0°$, for $r_g = 775$nm, 550 nm, and 225 nm; (b) angle of sidewall tilt of region I θ_1, for $r_g = 550$ nm, with amount of undercut $= 0\%$, 20%, and 50%; (c) θ_1, with amount of undercut $= 20\%$, for $r_g = 775$nm, 550 nm, and 225 nm. Symbols are for the numerical data from MAXWELL, dashed lines in (a) for analytical calculations from Eqs. (5c) and (6), and solid lines for curve connecting the numerical data. The dash-dotted lines are for the ratio of constriction resistance to total resistance R_c/R_{tot}.
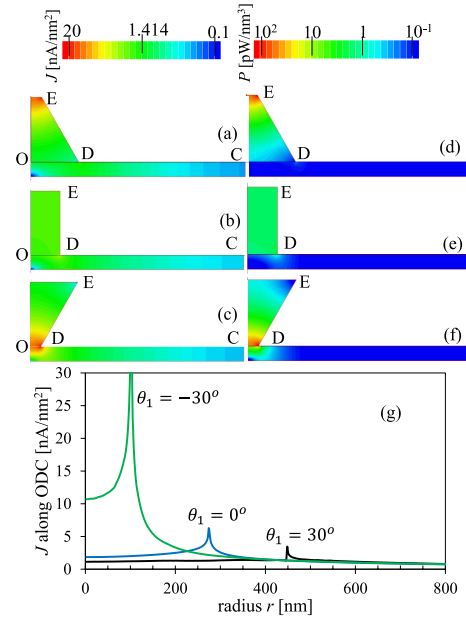

Fig. 8. (a)-(c) Current density distribution $J(r,z)$, and (d)-(f) the corresponding Joule heating power per volume $P(r,z) = \rho(r,z)J^2(r,z)$, for the vertical contact structure in Fig. 6 for $r_2 = 550$ nm and amount of undercut $= 50\%$. (a) and (d) are for the sidewall angle tilt $\theta_1 = 30°$, (b) and (e) for $\theta_1 = 0°$, and (c) and (f) for $\theta_1 = -30°$. (g) magnitude of current density along ODC for cases (a)-(c). In the calculation, we assume a total injection current of 0.5mA.

$r_g = 550$ nm and amount of undercut $= 50\%$. With zero sidewall tilt and uniform current distribution, the assumed injection current of 0.5mA corresponds to a current density of $J_0 = 2.1$ nA/nm^2 in region I. As shown in Fig. 8a, when $\theta_1 = 30°$, the current density is mostly crowed near the top boundary of region I, with current density as high as 28.5 nA/nm^2 at 1nm inwards from the rim point E, which is about 14 times J_0, and further, it is larger compared to that of vertical contact (Fig. 5a). On the other hand, the current

density near the interface between regions I and II become quite uniformly distributed. When $\theta_1 = 0°$ (Fig. 8b), the current density distribution near the top boundary of region I becomes almost uniform. The most current crowded region is near the constriction corner, point D, with a current density of 5.69 nA/nm^2 ($\sim 3J_0$) at 1 nm inwards from point D along the interface. When $\theta_1 = -30°$ (Fig. 8c), the current crowding region near the constriction corner D is greatly increased, with a current density as high as 28.4 nA/nm^2 at 1 nm inwards from point D, which is about 14 times J_0, much larger compared to that of vertical contact (Fig. 5c). The current density near point E is suppressed. The magnitude of current density along the contact interface ODC is shown in Fig. 8g for cases with different angle of tilt. It is important to note that even though the constriction resistance $R_c = 229\ \Omega$ for $\theta_1 = 30°$ and $R_c = 268\ \Omega$ for $\theta_1 = -30°$ are comparable (c.f. Fig. 7b), the location where current crowding occurs is very different. Figures 8d-f show the corresponding distribution of Joule heating power per volume $P(r, z) = \rho(r, z)J^2(r, z)$. The total Joule heating power in the structures in Figs. 8d-f is 458.8, 268.6, and 495.3 μW, respectively, corresponding to an increase of 71% for $\theta_1 = 30°$ and 84% for $\theta_1 = -30°$ relative to the straight sidewall case $\theta_1 = 0°$. The power density near the most current crowded region is significantly increased by the side wall tilt. The hottest spot follows closely the region of highest current density, yielding $P = 250$, 4.74 and 421 pW/nm^3 at 1nm away from the hottest corner for $\theta_1 = 30°$, $0°$, and $-30°$, respectively, corresponding to an increase of P by 52 times for $\theta_1 = 30°$ and by 88 times for $\theta_1 = -30°$ relative to the case $\theta_1 = 0°$. Note that the power density near the hottest spot is about one order of magnitude higher compared to that of vertical contact in Sec. II, for the same amount of undercut and same angle of sidewall tilt. While designs with θ_1 of $30°$ and $-30°$ produce power densities on the same order of magnitude, a design with $\theta_1 = -30°$ would affect the overall heating less for the nanolaser structure shown in Fig. 2, because the local heat can be quickly dissipated through the large-area substrate rather than through the gain region.

IV. CONCLUDING REMARKS

In this paper, we study the constriction resistance and current crowding in nanolasers. We examined both vertical contact and horizontal contact structures. The former is formed above the gain region, between the upper contact region and the upper pedestal region; whereas the latter is formed below the gain region, between the lower pedestal region and the bottom thin film layer. For the nanolaser structure under investigation, constriction resistance and the degree of current crowding in the bottom horizontal contact in nanolasers are much larger than those in the top vertical contact. The effects of nanolaser radius, amount of undercut, and angle of sidewall tilt are studied in detail. For both contact senarios, it is found that constriction resistance increases when the nanolaser radius decreases, the amount of undercut increases, or the angle (either positive or negative) of sidewall tilt increases. The current density distribution and the corresponding Joule

heating power density distribution are calculated, and the location where most current crowding and most Joule heating occur is identified. In the top vertical contact, when the pedestal sidewall tilt angle is positive, the hottest spot is located near the constriction corner at the interface between the top contact and the upper pedestal (points D and G in Fig. 3b); when the tilt angle is negative, the hottest spot is located near the bottom rim of the upper pedestal (points E and F in Fig. 3b). Because Joule heating in proximity to the gain region degrades the performance of gain medium, it is therefore more preferable to have a positive tilt angle for the top contact. In the bottom horizontal contact, when the sidewall tilt is positive, the hottest spot is near the top rim of the lower pedestal region (points E and F in Fig. 6b); when the sidewall tilt is negative, the hottest spot is near the constriction corner between the lower pedestal and bottom thin film (points D and G in Fig. 6b).
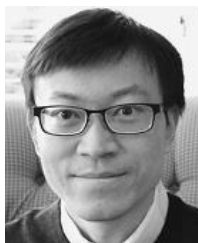
In the example nanolaser design in which only one pedestal sidewall tilt angle can be chosen, one needs to evaluate the opposite preferences for the upper and lower contacts. Firstly, at any given tilt angle, the upper vertical contact produces less heat power density than that from the lower horizontal contact; secondly, at any given power density, the larger heating from the lower contact can be efficiently removed via the substrate if it is generated close to the substrate. Negative tilt angle is thus preferred in order to reduce Joule heating in proximity to the gain region.

Future work may investigate the effects of contact resistance and current crowding on the threshold gain and efficiency of nanolasers. Because the bottom electrode is typically attached only to one side of the nanolaser (Fig. 2), it is important to study the asymmetric injection of charge carriers in nanolasers, which is expected to increase the resistance of the bottom contact and thin film significantly [24]. Coupled thermal-electrical conduction with temperature-dependent material properties is also of future interest.

REFERENCES

[1] C. Z. Ning, "Semiconductor nanolasers," *Phys. Status Solidi B*, vol. 247, no. 4, pp. 774–788, Apr. 2010.

[2] Q. Gu *et al.*, "Subwavelength semiconductor lasers for dense chip-scale integration," *Adv. Opt. Photon.*, vol. 6, no. 1, pp. 1–56, 2014.

[3] M. Smit, J. van der Tol, and M. Hill, "Moore's law in photonics," *Laser Photon. Rev.*, vol. 6, no. 1, pp. 1–13, Jan. 2012.

[4] S. Chu *et al.*, "Electrically pumped waveguide lasing from ZnO nanowires," *Nature Nanotechnol.*, vol. 6, no. 8, pp. 506–510, Aug. 2011.

[5] Y.-J. Lu *et al.*, "Plasmonic nanolaser using epitaxially grown silver film," *Science*, vol. 337, no. 6093, pp. 450–453, Jul. 2012.

[6] S. Arai, N. Nishiyama, T. Maruyama, and T. Okumura, "GaInAsP/InP membrane lasers for optical interconnects," *IEEE J. Sel. Topics Quantum Electron.*, vol. 17, no. 5, pp. 1381–1389, Sep. 2011.

[7] W. Zhou and Z. Ma, "Breakthroughs in photonics 2012: Breakthroughs in nanomembranes and nanomembrane lasers," *IEEE Photon. J.*, vol. 5, no. 2, Apr. 2013, Art. ID 0700707.

[8] F. Albert *et al.*, "Directional whispering gallery mode emission from Limaçon-shaped electrically pumped quantum dot micropillar lasers," *Appl. Phys. Lett.*, vol. 101, no. 2, p. 021116, Jul. 2012.

[9] K. Ding, M. T. Hill, Z. C. Liu, L. J. Yin, P. J. van Veldhoven, and C. Z. Ning, "Record performance of electrical injection sub-wavelength metallic-cavity semiconductor lasers at room temperature," *Opt. Exp.*, vol. 21, no. 4, pp. 4728–4733, Feb. 2013.

[10] Q. Gu *et al.*, "Amorphous Al$_2$O$_3$ shield for thermal management in electrically pumped metallo-dielectric nanolasers," *IEEE J. Quantum Electron.*, vol. 50, no. 7, pp. 499–509, Jul. 2014.

[11] C. Z. Ning, R. A. Indik, and J. V. Moloney, "Self-consistent approach to thermal effects in vertical-cavity surface-emitting lasers," *J. Opt. Soc. Amer. B*, vol. 12, no. 10, pp. 1993–2004, 1995.

[12] S. F. Yu, *Analysis and Design of Vertical Cavity Surface Emitting Lasers*. New York, NY, USA: Wiley, 2003.

[13] M. H. Shih *et al.*, "Identification of modes and single mode operation of sapphire-bonded photonic crystal lasers under continuous-wave room temperature operation," *Appl. Phys. Lett.*, vol. 90, no. 12, p. 121116, Mar. 2007.

[14] Q. Gu, J. S. Smalley, J. Shane, Y. Fainman, and O. Bondarenko, "Temperature effects in metal-clad semiconductor nanolasers," *Nanophoton. J.*, vol. 4, no. 1, pp. 26–43, 2014.

[15] T. Nakamura, T. Yamamoto, and S. Adachi, "Temperature dependence of lasing characteristics of irregular-shaped-microparticle ZnO laser," *Opt. Exp.*, vol. 23, no. 22, pp. 28905–28913, Nov. 2015.

[16] M.-K. Kim, Z. Li, K. Huang, R. Going, M. C. Wu, and H. Choo, "Engineering of metal-clad optical nanocavity to optimize coupling with integrated waveguides," *Opt. Exp.*, vol. 21, no. 22, pp. 25796–25804, Nov. 2013.

[17] J. Shane, Q. Gu, A. Potterton, and Y. Fainman, "Effect of undercut etch on performance and fabrication robustness of metal-clad semiconductor nanolasers," *IEEE J. Quantum Electron.*, vol. 51, no. 1, Jan. 2015, Art. ID 2000109.

[18] *MAXWELL 2-D Software*. [Online]. Available: www.ansys.com

[19] P. Zhang, Y. Y. Lau, and R. S. Timsit, "On the spreading resistance of thin-film contacts," *IEEE Trans. Electron Devices*, vol. 59, no. 7, pp. 1936–1940, Jul. 2012.

[20] P. Zhang, D. M. H. Hung, and Y. Y. Lau, "Current flow in a 3-terminal thin film contact with dissimilar materials and general geometric aspect ratios," *J. Phys. D, Appl. Phys.*, vol. 46, no. 6, p. 065502, Jan. 2013.

[21] P. Zhang and Y. Y. Lau, "Constriction resistance and current crowding in vertical thin film contact," *IEEE J. Electron Devices Soc.*, vol. 1, no. 3, pp. 83–90, Mar. 2013.

[22] J. Shane *et al.*, "Thermal considerations in electrically-pumped metallo-dielectric nanolasers," *Proc. SPIE*, vol. 8980, pp. 898027-1–898027-11, Mar. 2014.

[23] P. Zhang and Y. Y. Lau, "An exact field solution of contact resistance and comparison with the transmission line model," *Appl. Phys. Lett.*, vol. 104, no. 20, p. 204102, May 2014.

[24] P. Zhang, Y. Y. Lau, and R. S. Timsit, "Spreading resistance of a contact spot on a thin film," in *Proc. IEEE 59th Holm Conf. Elect. Contacts (HOLM)*, Sep. 2013, pp. 1–7.

Qing Gu received the B.A.Sc. degree from the University of British Columbia, Vancouver, BC, Canada, in 2008, and the M.S. and Ph.D. degrees from the University of California at San Diego (UCSD), La Jolla, CA, USA, in 2011 and 2014, respectively, all in electrical engineering. Since 2014, she has been a Post-Doctoral Researcher with the Ultrafast and Nanoscale Optics Group, UCSD. Her research interests include the fabrication and testing of semiconductor nanolasers, solid-state physics and quantum optics, novel nano-resonator design, and their insertion into photonic integrated circuits.

She has held undergraduate researcher positions with the Photonics Research Group, University of British Columbia, and the Canada's National Laboratory for Particle and Nuclear Physics, Vancouver.
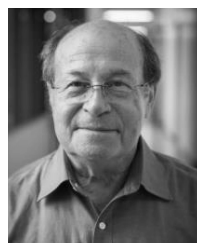
She was a recipient of the Undergraduate Student Research Award from the Natural Sciences and Engineering Research Council of Canada, and the Jacobs Bonus for Excellence Scholarship from UCSD.

Y. Y. Lau (M'98–SM'06–F'08) was born in Hong Kong. He received the S.B., S.M., and Ph.D. degrees in electrical engineering from the Massachusetts Institute of Technology (MIT), Cambridge, in 1968, 1970, and 1973, respectively. From 1973 to 1979, he was an Instructor and then an Assistant Professor of Applied Mathematics with MIT. He was with Science Applications Inc., McLean, VA, from 1980 to 1983, and the Naval Research Laboratory (NRL), Washington, DC, from 1983 to 1992, both as a Research Physicist. In 1992, he joined the Department of Nuclear engineering and Radiological Sciences, University of Michigan, Ann Arbor, as a Professor, and the Applied Physics Program.

He has worked on electron beams, coherent radiation sources, plasmas and discharges. He has over 220 refereed publications and holds 11 patents. He served as an Associate Editor of the *Physics of Plasmas* for three terms, and was a Guest Editor of the IEEE TRANSACTIONS ON PLASMA SCIENCE of the Special Issue on High-Power Microwave Generation. While at NRL, he won several Invention Awards and Publication Awards and was a recipient of the 1989 Sigma-Xi Scientific Society Applied Science Award. He became a fellow of the American Physical Society in 1986. He was a recipient of the 1999 IEEE Plasma Science and Applications Award.

Peng Zhang (S'07–M'12) received the B.Eng. and M.Eng. degrees in electrical and electronic engineering from Nanyang Technological University, Singapore, in 2006 and 2008, respectively, and the Ph.D. degree in nuclear engineering and radiological sciences from the University of Michigan (UM), Ann Arbor, in 2012. He is currently an Assistant Research Scientist with UM.

He has extensive publications on electrical contacts, classical and quantum diodes, Z-pinches, high power microwave sources, ultrafast electron emission, laser-plasma interaction, and most recently novel THz sources based on Smith–Purcell radiation and quantum tunneling plasmonics. His research interests are in nanoelectronics, electromagnetic fields and waves, lasers, and plasmas.

He was a recipient of the Richard and Eleanor Towner Prize for Outstanding Ph.D. Research, the Rackham Presidential Fellowship Award, the Best Presentation Award in the 2011 MIPSE Graduate Student Symposium, the UM Rackham Predoctoral Fellowship, and the IEEE Nuclear and Plasma Sciences Graduate Scholarship Award.

Yeshaiahu Fainman is currently a Cymer Professor of Advanced Optical Technologies and a Distinguished Professor of Electrical and Computer Engineering with the University of California at San Diego (UCSD), La Jolla, CA, USA, where he recently served as the Chair of the Department of Electrical and Computer Engineering.

He directs the research with the Ultrafast and Nanoscale Optics Group, UCSD, and has made significant contributions to near-field optical phenomena, inhomogeneous materials and metamaterials, nanophotonics and plasmonics, and nonconventional imaging. The research applications target information technologies and biomedical sensing. His current research interests are in near-field optical science and technology. He contributed over 220 manuscripts in peer-reviewed journals and over 350 conference presentations and conference proceedings.

He is a fellow of the Optical Society of America and the Society of Photo-Optical Instrumentation Engineers. He was a recipient of the Miriam and Aharon Gutvirt Prize, the Lady Davis Fellowship, the Brown Award, and the Gabor Award.